Materials and Design 196 (2020) 109123

Contents lists available at ScienceDirect

Materials and Design

journal homepage: www.elsevier.com/locate/matdes

Development and application of interatomic potentials to study the stability and shear strength of Ti/TiN and Cu/TiN interfaces

Abu Shama Mohammad Miraz [a], Nisha Dhariwal [a], W.J. Meng [b], Bala R. Ramachandran [a], Collin D. Wick [a,*]

[a] College of Engineering & Science, Louisiana Tech University, Ruston, Louisiana 71272, USA
[b] Department of Mechanical & Industrial Engineering, Louisiana State University, Baton Rouge, Louisiana 70803, USA

HIGHLIGHTS

- Modified embedded atom method interatomic potentials were developed to study Cu/TiN and Ti/TiN interfaces.
- The model was parameterized to high-fidelity γ-surfaces of the interfacial slip planes using a newly developed genetic parameterization scheme.
- Stable Cu/TiN and Ti/TiN interfaces with misfit dislocation networks were detected with the model.
- Shear strength calculated with the model for Ti/TiN and Cu/TiN agree well with the experimental results.

GRAPHICAL ABSTRACT

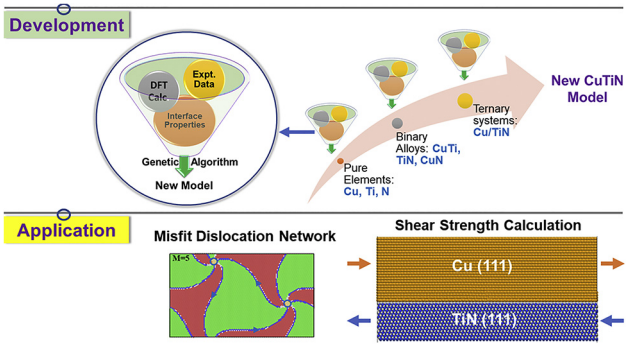

ARTICLE INFO

Article history:
Received 8 June 2020
Received in revised form 2 September 2020
Accepted 3 September 2020
Available online 08 September 2020

Keywords:
2NN-MEAM
Metal/ceramic interfaces
Shear strength
Semi-coherent interfaces
Genetic algorithm
Misfit dislocation networks
Molecular dynamics simulation

ABSTRACT

A modified embedded atom method interatomic potential was developed to study semi-coherent metal/ceramic interfaces involving Cu, Ti and N. A genetic algorithm was used to fit the model parameters to the physical properties of the materials. To accurately describe interfacial interactions and shear, two-dimensional generalized stacking fault energy profiles for relevant slip systems were selected as one of the major parameterization targets for the models. The models were applied to study semi-coherent Ti(0001)/TiN(111) and Cu(111)/TiN(111) systems. Ti/TiN was stable with misfits accommodated away from the interface. Cu/TiN, in contrast, was more stable with misfits at the interface. A spiral pattern in the misfit dislocation networks was observed away from the Cu/TiN interface, similar to the metal/metal (111) semi-coherent interfaces. The theoretical shear strength calculated for Ti/TiN when the misfits were several layers away from the interface and for Cu/TiN with the misfit at the chemical interface, had reasonable agreement with experiment.

1. Introduction

Many technological applications use engineered components and systems that contain metal/ceramic interfaces to enhance their applicability [1]. Examples of such applications and materials are mechanical parts in automobiles, aero-engines, gas turbines, fuel cells, cutting and machining tools; components of micro and optoelectronic circuits used in sensors and actuators etc. [2–7]. In many of these cases, proper functioning of components over long time periods requires strong adhesion and high mechanical strength of these metal/ceramic interfaces. It is essential to understand the energetics and

* Corresponding author.
E-mail address: cwick@latech.edu (C.D. Wick).

https://doi.org/10.1016/j.matdes.2020.109123

mechanical properties of these interfaces in relation to the interfacial structures such as misfit dislocations and orientation relations so that interfaces that meet required engineering specifications can be designed based on sound physics and materials science principles, instead of the traditional trial-and-error approach.

A diverse array of metal/ceramic interfaces have been studied by both experimental and computational researchers over the last two decades [6,8–17]. TiN, in particular, is often the coating of choice in environments involving high temperatures and pressures due to its high hardness and low thermal conductivity [18,19]. Thin metal interlayers such as Ti are often sandwiched between TiN and the substrate to improve the overall adhesion of the coating [20–24]. However, Ti/TiN is characterized by weak interactions near the interface that leads to unstable shear-off [25]. For Cu/TiN interfaces, which are commonly found in the metallization of microelectronic circuits, promoting strong interfacial adhesion remains a challenge [26,27].

The experimental procedures to quantify interfacial interactions and mechanical response of metal/ceramic interfaces often involve some form of disruption or deformation to the interface being examined [28,29]. With increases in the availability of modern high-performance computing resources, computational approaches are becoming a popular tool for investigating metal/ceramic interfaces [30]. In that regard, quantum mechanical calculations, such as density functional theory (DFT), can be highly accurate, but lack in scalability due to their high computational cost. To observe the impact of interfacial structures, such as misfit dislocation network geometries and orientation relationships, on interfacial mechanical properties, a much larger size is required than what is feasible with DFT. Molecular dynamics (MD) simulations with interaction potentials can be applied to systems large enough to capture a moderate range of physical phenomenon key to understanding these interfaces [31–34]. The challenge in these simulations is the limited availability of reliable interatomic potential models.

While there are reports of interatomic potentials for several unary and binary systems of Cu, Ti and N [35–39], to the best of our knowledge, there is no interatomic potential model available for all three together. To describe the interactions between these elements with a common mathematical formalism is a challenging task because of their widely varying physical characteristics, manifested in the differences in crystal structure and phases formed. The modified embedded atom method (MEAM), originally developed by Baskes et al. [40–42], is a semi-empirical interatomic potential that improves upon the older embedded atom model [43] by incorporating the angular dependency to the host electron density. In a later modification to the MEAM, the interaction between atoms were extended to the second nearest neighbors for a better description of BCC metals [44–46]. These potentials have been used to describe a variety of unary, binary, and ternary alloys, along with TiN interactions [36,37,44,45,47]. The lack of interatomic potential for CuTiN can be addressed by building new MEAM potentials that closely follow the relevant physical properties of the constituent elements and their alloys.

In this work, MEAM potentials for pure Cu and Ti, along with CuTi, TiN, CuN, and CuTiN systems were developed with a focus on metal/ceramic interfaces. The new model was then applied to energy calculations and shear loading simulations on Ti/TiN and Cu/TiN bilayer systems with approximately 10 nm thickness in different interfacial coherency and misfit scenarios.

2. Methodology

2.1. MEAM formalism

The mathematical details for the MEAM formalism are well established and not within the scope of this text [41]. Briefly, the total energy of a system is given as,

$$E_{\text{total}} = \sum_i \left[F_i(\overline{\rho}_i) + \frac{1}{2} \sum_{i \neq j} S_{ij} \varphi_{ij}(R_{ij}) \right], \tag{1}$$

where F_i is the embedding function, and φ_{ij} is the pair potential for atoms i and j, separated by a distance, R_{ij}. S_{ij} is the many-body screening function and is limited by the C_{min} and C_{max} parameters. The background electron density $\overline{\rho}_i$ is composed of s, p, d and f partial electron density contributions combined by adjustable weighting factors ($t_i^{(h)}$,h = 0–3) [47]. The atomic electron density associated with each partial electron density have the following form,

$$\rho^{a(h)} = \rho_0 \exp\left[-\beta^{(h)} (R/\mathrm{r}_e - 1) \right], \tag{2}$$

where ρ_0 is the atomic electron density scaling factor, $\beta^{(h)}$ are adjustable decay lengths and r_e is the nearest-neighbor distance in the reference structure. The functional form of embedding function is given by,

$$F(\rho_i) = AE_C \left(\rho/\rho^0 \right) \ln \left(\rho/\rho^0 \right), \tag{3}$$

where A is an adjustable parameter, E_C is the cohesive energy, and $\overline{\rho}^0$ is the background electron density of the reference structure. The pair potential is not assigned a functional form, but is obtained from the known values of total energy per atom and the embedding energy of the reference structure. The total energy per atom as a function of nearest neighbor distance, R, is calculated using Rose's universal equation of state given by [48],

$$E^{\mu}(R) = E_C \left(1 + a^* + da^{*3} \right) e^{-a^*}, \tag{4}$$

where $a^* = \alpha(R/r_e - 1)$ and $\alpha = (9B\Omega/E_C)^{1/2}$, B is the bulk modulus, Ω is equilibrium atomic volume, and d is an adjustable parameter.

For pure elements, the MEAM formalism has 15 adjustable parameters. As evident from Eq. (4), four of these parameters (E_C, r_e, α and d) are associated with the universal equation of state. There are eight parameters for electron density which are the exponential decay lengths $\beta^{(h)}$, (h=0–3) and the weight factors $t_i^{(0)}$, $t_i^{(1)}$, $t_i^{(2)}$and $t_i^{(3)}$. The embedding function has one parameter, A, and the many-body screening function has two parameters, C_{min} and C_{max}.

For binary alloys, 13 independent model parameters must be defined in addition to the ones for the pure elements [35,49]. Like the pure elements, there are four parameters (E_C, r_e, α and d) related to the universal equation of states applied to the binary reference structure. When determining the many-body screening factors, S_{ij}, up to three different atom types need to be taken into account. As a consequence, multiple C_{min} and C_{max} parameters are considered. These include four of each (eight total) for binary interactions and an additional three of each (six total) for ternary interactions [47,50]. The other parameter is the atomic electron density factor, ρ_0.

2.2. Algorithm for parameter fitting

In order to fit the MEAM parameters to a set of properties obtained either from experimental results or DFT (in the case of the unavailability of the former), an in-house python code was developed as outlined in Fig. 1. The array of parameters {Θ} were optimized using a simple minimization procedure in conjunction with a genetic algorithm. At the start of each minimization cycle, a specific MEAM parameter, Θ_i, was chosen randomly. There was a pre-set maximum displacement δ_i for each parameter, Θ_i, typically up to 10% of its absolute value. Four trials were created for the randomly selected parameter by choosing five equidistant values spanning from (Θ_i - δ_i) to (Θ_i + δ_i). The properties were calculated for each trial, ρ_j^{trial}, and compared with their target values obtained from DFT/experiment, ρ_j^{target}. Then, the mean squared objective function, $J^{\text{trial}}(\Theta_i)$, in Eq. (5) was calculated for each of the four trials,

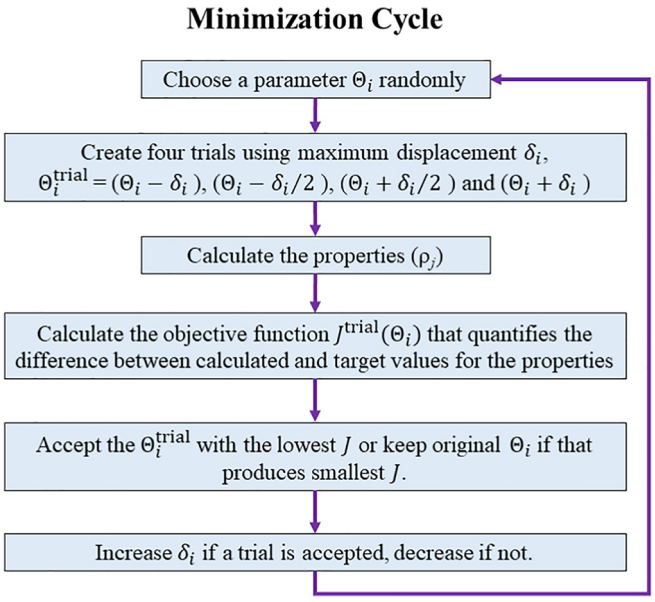

Fig. 1. Minimization procedure used for a given parameter set.

$$J^{trial}(\Theta_i) = \sum_j \omega_j \times \left(\rho_j^{trial} - \rho_j^{target}\right)^2, \quad (5)$$

where ω_j is an arbitrary weight assigned to each property, ρ_j. This function is summed over all the properties, and the trial with the minimum value of $J^{trial}(\Theta_i)$ was accepted. When a trial was accepted, the δ_i for that parameter was increased. If none of the four produced a smaller J^{trial} than the original value, no changes occurred, and the δ_i for that parameter was decreased.

The minimization scheme discussed above converges quickly for any given parameter set. However, it is prone to stagnation in local minima for the parameters. To address this, a genetic algorithm was used in conjunction with the minimization scheme that allows for a search through a broader spectrum of parameter space. Fig. 2 outlines the genetic algorithm used for this work. Six parameter sets, denoted by S_1, S_2, S_3, S_4, S_5 and S_6, were simultaneously optimized as described in Fig. 1 for 50 cycles each. Parameter sets from existing models as well as sets that were randomly generated made up the initial six sets. After 50 minimization cycles, the parameter set with the smallest value of J was selected as S_{min}. Sets having J values larger than $10 \times J_{min}$ (cost function of S_{min}) were destroyed. Also, parameter sets that were close to the parameters of S_{min}, (their mean squared difference being within a cut-off of 0.1) were also destroyed.

The destroyed sets were substituted by new sets created either by mating or mutating surviving sets. Two sets were mated by taking the average of their Θ parameters, while mutations were done by randomly modifying S_{min} up to ±20% to create new sets of parameters. For instance, if three sets survived, two new sets were created by mating, and one created by mutation. At least 20 such genetic algorithm cycles (1000 total minimization cycles) were run and the parameter sets often converged to very small values of J.

2.3. Parameter optimization for this work

For the present work, the parameter set for pure N were taken from Lee et al. without modification [35]. Parameters for pure Ti and Cu were taken from existing literature as initial values [37,38] along with five additional sets, each randomly modified, to start the fitting procedure outlined in Section 2.2. Among the fifteen parameters discussed above for pure elements, cohesive energy (E_C) and nearest-neighbor distance (r_e) of the reference structure were taken from available experimental values, d is fixed to zero for a simpler version of Rose equation [48],

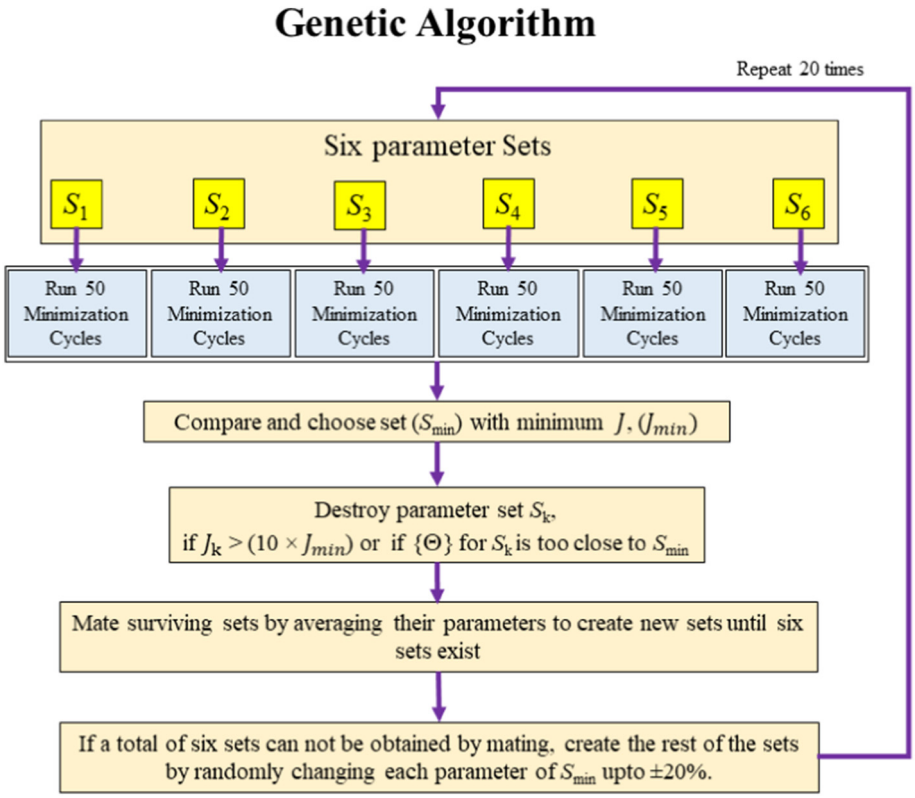

Fig. 2. Genetic Algorithm used to find the optimum parameter set.

$t_i^{(0)}$ is set to unity at equilibrium without loss of generality. Eleven parameters (α, $\beta^{(0)}$, $\beta^{(1)}$, $\beta^{(2)}$, $\beta^{(3)}$, $t_i^{(1)}$, $t_i^{(2)}$, $t_i^{(3)}$, A, C_{min} and C_{max}) were fit to several physical properties of the pure elements (more on these physical properties in Section 2.4).

Once the pure elements were parameterized with satisfactory reproduction of the physical properties, those parameters were used for modeling the binary alloys. Eleven binary parameters (four C_{min} and four C_{max}, α, E_C, r_e) were adjusted in this work for each binary combination. For TiN and CuN binary alloys, NaCl-type reference structures were considered, while for CuTi a B2-type structure was taken as reference, and the parameters associated with the reference structures (α, E_C, r_e) were fit as well. For CuTiN ternary systems, three additional C_{min} and C_{max} parameters were fit to the physical properties of Cu/TiN metal/ceramic systems.

2.4. Calculation of properties

The pure elements were fit to physical properties such as lattice constants, elastic constants, monovacancy formation energy (E_{vac}), surface energies (E_S), solid density at 298 K (ρ_{298K}), energy ratio of different phases (E/E_0) with respect to the minimum energy phase (E_0), and generalized stacking fault energies (GSFEs) along different planes. The binary and ternary parameters were also fit to a range of properties, namely lattice constants and enthalpies of mixing ($\Delta_{mix}H$) of different phases, surface energies (E_S), elastic constants, work of adhesion (WoA), and GSFEs of specific interfaces. The experimentally available values for these properties were obtained and set as target values for fitting. In cases where a property value was not readily available from experiment, the DFT-calculated values were used as target values for fitting. E_{vac} were calculated by removing one atom from a system. For surface energy calculations, the box for bulk systems were elongated in the direction normal to the surface of interest, creating two vacuum/solid interfaces. E_S was given by,

$$E_S = (E_{Slab} - E_{Bulk})/(2 \times \text{Area}), \tag{6}$$

where, E_{Slab} and E_{Bulk} are the energies of the system with vacuum/solid interface and the bulk system, respectively. The $\Delta_{mix}H$ for binaries were calculated as follows,

$$\Delta_{mix}H = (E_{total} - n\varepsilon_a - m\varepsilon_b)/(n+m), \tag{7}$$

where, E_{total} is the energy of a system with n number of a type atoms and m number of b type atoms. ε_a and ε_b are the energy per atom for a and b type atoms in their bulk structures. The WoA for metal/ceramic interfaces were obtained using the following formula,

$$\text{WoA} = (E_m + E_c - E_{mc})/\text{area}, \tag{8}$$

where E_m, E_c and E_{mc} are the optimized energies of the relaxed metal, ceramic and metal/ceramic combinations, respectively.

The GSFE for a particular glide plane (denoted P) was mapped out by moving all the atoms above the plane in concert in the X and/or Y directions, while fixing all the X and Y atomic positions below. Such movements were carried out along X and Y in 10 steps, covering up to half the cell length in both directions. The 10×10 points sampled inside a quadrant of the surface area in this manner, were then replicated in X and Y corresponding to the symmetry of the atomic positions at the plane. For each of the 100 configurations, an energy minimization was performed by allowing atomic positions to relax in Z while fixing their X and Y positions. Interfaces that had more complex symmetry in atomic positions required a different fraction of the area (than just a quadrant) to be replicated to produce a full GSFE surface. Once the full GSFE was mapped out, the minimum energy path was identified along the X direction. Further details are in our previous work [51,52].

2.4.1. DFT calculations

DFT calculations were performed using the Vienna Ab-Initio Simulation Package (VASP) package using the Perdew, Burke and Ernzerhof (PBE) generalized gradient approximation for the exchange-correlation functional [53–55]. The Projector Augmented Wave (PAW) pseudopotentials were used for core electrons [54,55], and the valence electrons were expanded by a plane wave basis set with a cutoff energy of 400 eV. The Monkhorst-Pack scheme was used for sampling the k-point of the plane wave basis in the first Brillouin zone [56]. E_S, E_{vac}, $\Delta_{mix}H$, E/E_0, elastic constants, WoA, and GSFEs were calculated using DFT. The values obtained from DFT that were used for fitting are listed in the Section 3. The DFT systems were generally limited to 200 atoms due to the large computational cost associated with systems larger than that.

2.4.2. Details of calculations for MEAM potential fitting

The MD calculations with MEAM potentials were carried out using the LAMMPS package [57]. Structural relaxation and energy minimization were performed in evaluating $\Delta_{mix}H$, lattice and elastic constants, E_{vac}, E_S, and WoA calculations. In order to facilitate a convenient comparison between the energies of different surfaces of a particular element/alloy, the size of the systems was kept close to one another both in terms of number of atoms and length of X and Y dimensions. For solid density calculations of pure metals at 298 K, systems having more than 250 atoms were used. We also carried out a calculation for a larger system with 6500 atoms and no significant changes in the results were observed with systems larger than that. These calculations were carried out for 20 ps with a 1 fs timestep, and performed in the NPT ensemble with the temperature and pressure being controlled by Nosè-Hoover thermostat and barostat [58,59]. In addition to the model developed for this work, comparisons are made with existing MEAM models for Ti developed by Lee et al. (denoted Lee model) [36], Cu developed by Baskes et al. (denoted Baskes model) [37], and TiN also developed by Kim et al. (denoted Kim model) [38]. To our knowledge, no models for Cu/TiN currently exist in the literature so we are unable to make direct comparisons with others.

2.4.3. Details for large scale MD simulations

Energetics and the shear strength for semi-coherent Ti/TiN and Cu/TiN were evaluated using the newly developed models. As used in previous reports [25], two orientational relations considered for Ti/TiN are,

$$\text{OR1}: X \| \left[11\bar{2}0\right]_{Ti} \| \left[1\bar{1}0\right]_{TiN};\ Y \| \left[\bar{1}100\right]_{Ti} \| \left[11\bar{2}\right]_{TiN} \text{ and } Z \| [0001]_{Ti} \| [111]_{TiN}, \tag{9}$$

and

$$\text{OR2}: X \| \left[\bar{1}\bar{1}20\right]_{Ti} \| \left[1\bar{1}0\right]_{TiN};\ Y \| \left[1\bar{1}00\right]_{Ti} \| \left[11\bar{2}\right]_{TiN} \text{ and } Z \| [0001]_{Ti} \| [111]_{TiN} \tag{10}$$

For Cu/TiN, semi-coherent structures with the following experimentally observed [60–63] orientational relation was considered,

$$X \| \left[1\bar{1}0\right]_{Cu} \| \left[11\bar{2}\right]_{TiN};\ Y \| \left[11\bar{2}\right]_{Cu} \| \left[1\bar{1}0\right]_{TiN} \text{ and } Z \| [111]_{Cu} \| [111]_{TiN} \tag{11}$$

The lengths of the X and Y dimensions were chosen to minimize the strain caused by lattice mismatch between the metal and ceramic at the interface. As such, the X and Y lengths were 16.1 nm and 27.9 nm, respectively, for Ti/TiN, whereas for Cu/TiN, they were 17.1 nm and 29.6 nm. The total thickness of the metal/ceramic bilayers were around 8 nm with approximately 5 nm thick metal placed on top of 3 nm thick ceramic. The interfacial structures were relaxed in two steps: a finite temperature (10K) relaxation for 50 ps at constant volume and an iterative stress-relieve treatment to minimize the normal stress components. During each relaxation step, the top and bottom two layers

Table 1
Parameter sets for pure elements. Units of E_C and r_e are in eV and Å, respectively.

	E_C	r_e	α	A	$\beta^{(0)}$	$\beta^{(1)}$	$\beta^{(2)}$	$\beta^{(3)}$	$t_i^{(1)}$	$t_i^{(2)}$	$t_i^{(3)}$	C_{min}	C_{max}
N	4.88	1.10	5.96	1.80	2.75	4.00	4.00	4.00	0.05	1.00	0.00	2.00	2.80
Ti	4.87[a]	2.92[a]	4.41	1.19	1.58	0.08	2.89	0.0016	5.55	6.79	−2.05	0.89	2.85
Cu	3.54[b]	3.61[b]	4.82	0.91	3.68	4.30	5.75	0.12	2.32	6.94	6.00	0.51	1.92

[a] Reference [38].
[b] Reference [37].

were fixed in the Z direction, but allowed to relax in X and Y. Once the atomic positions were minimized, their respective dimensions (X, Y, and Z) were adjusted to minimize the stress in their specific directions. Similar relaxation procedure was used in previous studies [25,64]. The normal stress components were less than 100 Pa after the relaxation. The interfacial energy was calculated using the following formula,

$$\gamma = {}^1\!/_A(E_{\text{interface}} - nE_{\text{metal}} - mE_{\text{TiN}}), \tag{12}$$

where $E_{\text{interface}}$ is the energy of the total bilayer system, A is the area of the interface calculated from the in-plane X and Y dimensions of the interface. The values of n and m are the number of metal atoms (Ti or Cu) and the number of TiN, respectively. E_{metal}, and E_{TiN} are the cohesive energies of metal (Ti or Cu) and TiN, respectively.

To estimate the theoretical shear strength of the interfacial systems, stress-controlled shear loading was quasi-statically applied in the X direction. Incremental deformation gradients were applied for individual metal and ceramic phases according to their elastic constants, followed by constant volume relaxation at 5 K for 1 ps. Finally, energy minimization was carried out with the conjugate gradient method. Theoretical shear strength was estimated using similar methods in prior studies [25,64,65].

3. Results and discussion

3.1. Pure elements

As mentioned earlier, the parameter for pure N were taken from Lee et al. without modification (See Table 1), where the reference structure was a dimer [35]. The parameter values acquired after fitting for pure Ti and pure Cu are given in Table 1. FCC and HCP were the reference structures for Cu and Ti, respectively. E_C and r_e were fixed to the experimental values for Cu and Ti.

For Ti and Cu, a comparison of the experimental/DFT-calculated values and those derived from new and existing MEAM models are given in Table 2. The phases denoted with E_1 and E_2 are identified with the values given in the table for both the pure elements with respect to the most stable phases for the individual metals (E_0). All of these properties were included in the new model's parameterization. As is evident, generally good agreement was achieved with the targeted properties for both the existing and the newly developed MEAM models.

Of particular interest for shear properties of metals is their GSFE, the calculation of which is described in the previous section. The Ti model was fit to the γ/GSFEs of basal (0001), prismatic $\left(10\bar{1}0\right)$ and pyramidal $\left(10\bar{1}1\right)$ slip planes of HCP Ti. GSFEs calculated with DFT, the Lee model [36], and our model are illustrated in Fig. 3(a-c) for the basal plane, and in Fig. S1 in the supplementary material for the prismatic and pyramidal planes. While both models reproduced the low-energy stable regions fairly well, our model more closely reproduced the entire GSFE surface, especially the high-energy regions. The minimum energy path on these GSFEs plotted as a function of position in the $\left[\bar{1}\bar{1}20\right]$ direction for all three cases is shown in Fig. 3(c-e). For the basal plane, both models showed similar amplitudes (barrier height) as with DFT, but the stacking fault at around X = 1.5 Å was more stable with our model than DFT. Although both models overestimated the prismatic slip barrier, the pyramidal slip barrier agreed well with the DFT.

For Cu, GSFEs of (001) and (111) were fit to the model. GSFEs of Cu (001) and Cu(111) calculated with DFT, the Baskes model [37], and our model are shown in Fig. 4. Clearly, the features attained in the DFT map was accurately reproduced by the new model. For both the surfaces, the barrier height from the new model shown in Fig. 4(d) agrees very well with DFT, while the barrier height with the Baskes model is off by around 0.2 J/m^2 from DFT.

3.2. Binary alloys

Once the pure elements were parameterized, the binary parameters for TiN, CuTi, and CuN were fit to their corresponding properties. The values of the binary parameters reached after fitting are listed in Table 3 for TiN, CuTi and CuN binary systems. The scaling parameter, ρ_0 was kept fixed for these calculations so that $\rho_0^{\text{N}}/\rho_0^{\text{Ti}} = \rho_0^{\text{N}}/\rho_0^{\text{Cu}} = 18$, as had been done previously [38].

Table 2
Comparison of the DFT calculated or experimental properties of Cu and Ti with values obtained using existing models and the newly developed model in this work.

Properties	Ti			Cu		
	Expt/DFT	Lee [36]	New Model	Expt/DFT	Baskes [37]	New Model
E_{vac} (eV)	1.27[a], 1.55[a]	1.75	1.57	1.03[b], 1.19[c]	1.12	1.62
E_S (001) (J/m^2)	2.10[d], 1.92[e]	2.14	1.88	1.46[*], 1.44[f] 1.44[g]	1.82	1.42
E_S (110) (J/m^2)				1.54[*], 1.55[g]	1.74	1.56
E_S (111) (J/m^2)				1.27[*], 1.30[f], 1.29[g]	1.52	1.30
E_1/E_0	0.9570[*] (E_1 → BCC)	0.9956	0.954	0.9895[*] (E_1 → BCC)	1.0000	0.9968
E_2/E_0	0.9820[*] (E_2 → FCC)	0.9906	0.997	0.9938[*] (E_2 → HCP)	0.9964	0.9987
ρ_{298K} (g/cm^3)	4.51[h, j]	4.48	4.48	8.96[i], 8.93[h]	8.79	8.83
C_{11} (GPa)	162.4[j], 176.1[k]	170.4	163.5	168.3[l]	172.5	157.8
C_{12} (GPa)	92.0[j], 86.9[k]	80.4	68.0	122.1[l]	121.9	107.7
C_{13} (GPa)	69.0[j], 68.3[k]	74.8	54.7			
C_{33} (GPa)	180.7[j], 190.5[k]	187.1	180.1			
C_{44} (GPa)	46.7[j], 50.8[k]	42.1	43.8	75.7[l]	76.1	100.1
C_{66} (GPa)	35.2[j], 44.6[k]	44.8	47.8			

[*] DFT calculated in the present work.
[a] Reference [66].
[b] Reference [67].
[c] Reference [68].
[d] Reference [69].
[e] Reference [70].
[f] Reference [71].
[g] Reference [37].
[h] Reference [72].
[i] Reference [73].
[j] Reference [74].
[k] Reference [75].
[l] Reference [76].

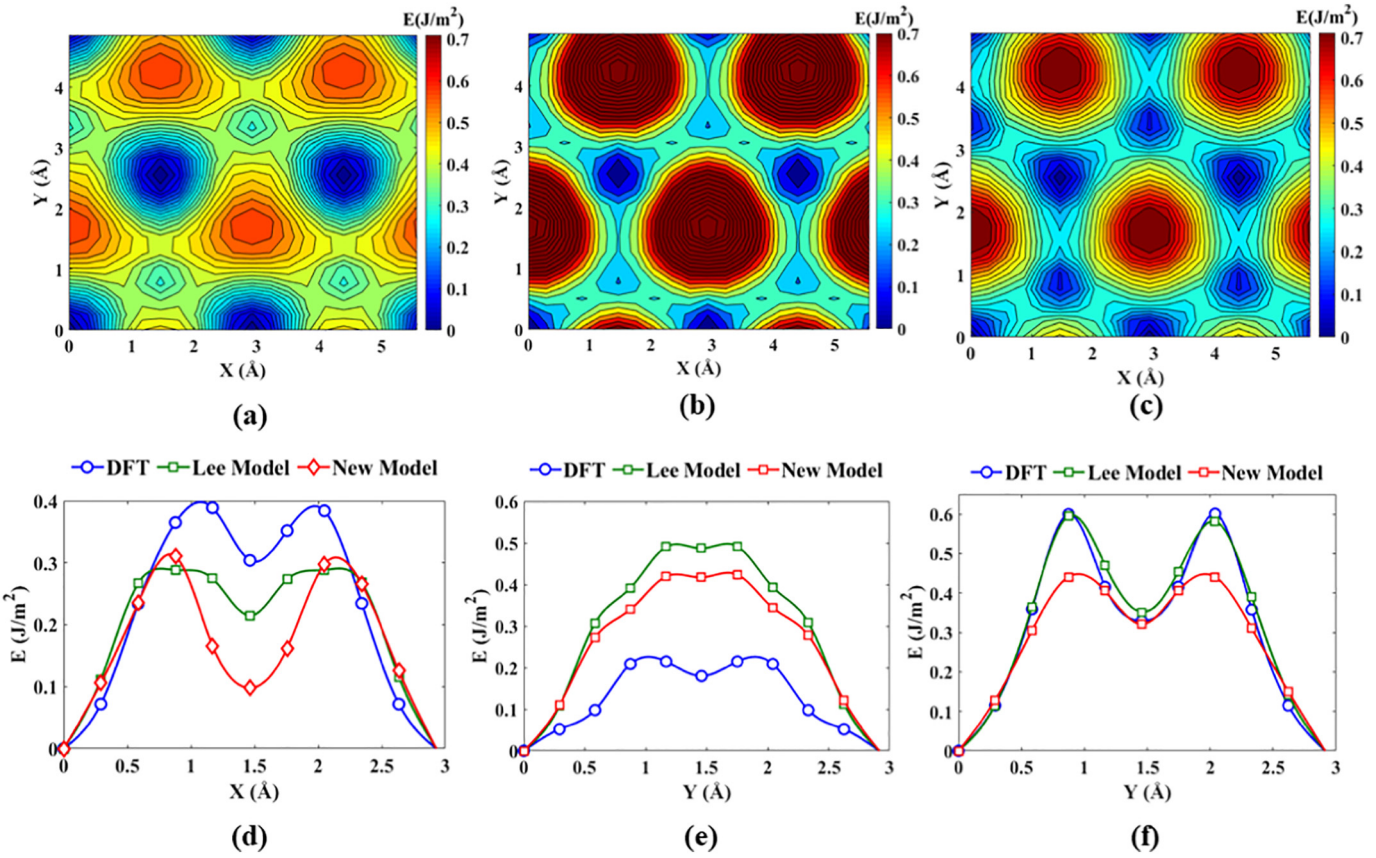

Fig. 3. GSFEs of the basal slip plane calculated using (a) DFT, (b) existing Lee model [36] and (c) our model. Minimum energy paths extracted from the GSFEs plotted against the minimum energy direction for (d) basal, (e) prismatic and (f) pyramidal slip planes.

3.2.1. TiN binary systems

The phase diagram for TiN binary systems shows the NaCl-type TiN phase being the most stable at room temperature, with a stable intermediate phase of Ti_2N [38,77]. Therefore, the experimental values of relevant properties such as lattice constants, elastic constants, surface energies for these phases were set as targets for the model. To facilitate the transferability of the model to the metal/ceramic systems, DFT-calculated features involving the Ti(0001)/TiN(111) interfacial systems, such as work of adhesion and GSFEs, were also used in the fitting. Table 4 lists the properties utilized in the fitting procedure, along with the target and the reproduced values for those properties. In the same table, the values are also compared with the ones obtained from Kim et al. (Kim model) [38].

Lattice constants reproduced by both the new model and the Kim model were in good conformity with experimental values for both TiN and Ti_2N phases, while the values reached for $\Delta_{mix}H$ correctly indicated that the NaCl-type TiN was the more stable phase of the two. There was a general agreement to the elastic constants and the surface energies experimentally calculated for the TiN phase. Particularly, the order of the surfaces in terms of their stability, $(001) < (110) < (111)$, were suggested accurately by both models. The Ti(0001)/TiN(111) system was created by putting a (2×1) Ti system comprising of 64 atoms on top of a (2×1) TiN system of 48 atoms. To assure that only one interface between the metal and the ceramic were being considered, at least 15 Å of vacuum were present inside the simulation box in the direction perpendicular to the interface creating two solid/vacuum interfaces. DFT calculations of these systems are described in our previous works [51,52]. With the new model, the WoA at the chemical interface (where the Ti atomic layer from Ti-phase comes in contact with the N layer from the TiN phase) is in good agreement with the DFT value.

GSFEs were calculated between the Ti(0001) and TiN(111) interfaces, and the results for DFT, the Kim model [38], and the new model are given in Fig. 5(a-c). As the GSFEs clearly reveal, the Kim model gave much higher energy in the unstable region than our model while the lower energy regions were reproduced well by both the MEAM models. From this point forward, the atomic layers near the interface will be denoted with M and the plane between the layers with P. As illustrated in Fig. 5(d), the chemical interface where the N layers from the ceramic meets with the first Ti atomic layer ($M = 1$) from the Ti-phase is marked as $P = 0$. The next Ti atomic layers, and the planes between them are marked with subsequent numbers. The barrier height for $P = 0$ with the new model agrees with the DFT value as shown in Fig. 5(e). However, the barrier height with the Kim model was almost double that of DFT. For $P = 1$, the stacking fault energy at $X = 1.5$ Å was accurately reproduced by both the models [see Fig. 5(f)]. However, both models overestimated the barrier height compared to DFT.

3.2.2. CuTi binary systems

Several CuTi intermetallic phases have been reported in the literature such as CuTi, Cu_2Ti, Cu_3Ti, Cu_4Ti, $CuTi_2$, Cu_3Ti_2, and Cu_4Ti_3 [82–91]. The reference structure chosen is a perfectly ordered hypothetical B2-type system where the second nearest neighbor is of the same type. To fit the binary parameters to the properties of CuTi alloys, four real phases were chosen from the phase diagram having four different types of structures, namely γ-CuTi ($D^7_{4h}P4/nmm$) [39], $CuTi_2$ ($D^1_{4h}I4/mmm$) [92], Cu_3Ti ($D^{13}_{2h}Pmmn$) [85], β-Cu_4Ti ($D^{16}_{2h}Pnma$) [89]. Among these four phases γ-CuTi is the most stable phase followed by $CuTi_2$ at 298 K [86]. Since these are equilibrium phases, some of their properties such as lattice constants and enthalpy of formation are available from experiments [83–87]. We obtained the

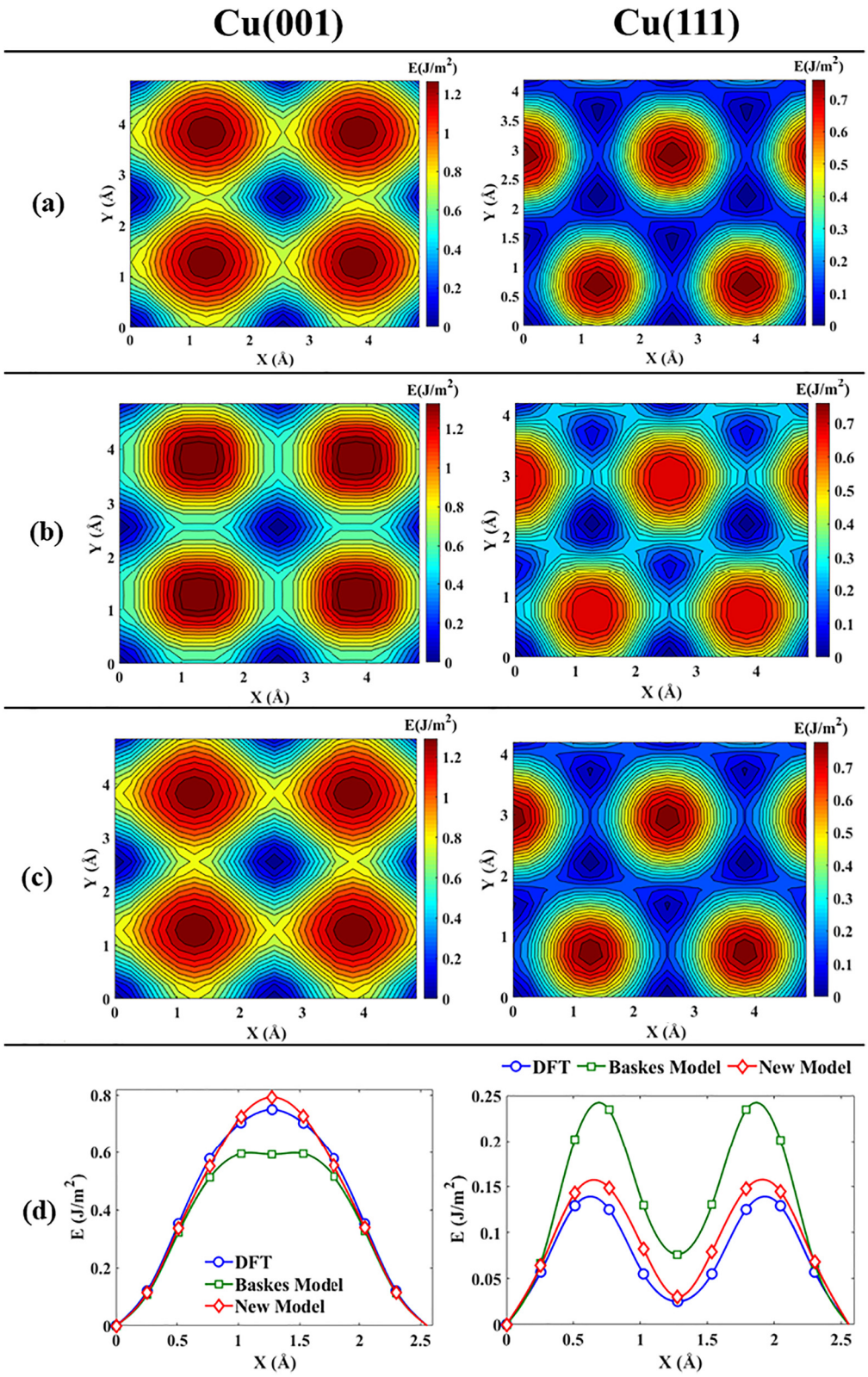

Fig. 4. GSFEs of Cu(001) and Cu(111) calculated using DFT (row a), existing Baskes models [37] (row b) and the new model (row c). The minimum energy paths obtained from the GSFEs of are compared in row d.

elastic constants and the surface energies of the most stable γ-CuTi phase from our DFT calculations.

Table 5 gives a comparison between the DFT/experiment and the new model, along with a model from Kim et al. [39] (Kim model) for a variety of CuTi properties. Lattice parameters calculated by the optimized model conformed to the target values to a moderate degree. The order of phase stability as suggested by our DFT results as well as previous reports was correctly reproduced by the model as γ-CuTi > $CuTi_2$ [90]. For the most stable phase γ-CuTi, the stability of different surfaces was reproduced in the same order as DFT (001> 111 > 110)

Table 3
Optimized parameters for binary systems. In any pair, the two elements are denoted by i and j, respectively in C parameters such that $C_{min}(\mathbf{Ti-Ti-N})$ is denoted by $C_{min}(i-i-j)$ for TiN.

Parameters	$(i-j)$ pair		
	TiN	CuTi	CuN
E_C	6.6139	4.4028	4.6872
r_e	2.1195	2.6585	1.9846
α	4.7225	3.7617	9.8671
$C_{min}(i-i-j)$	0.4263	0.3	0.7883
$C_{min}(j-j-i)$	1.0733	1.034	0.9997
$C_{min}(i-j-i)$	1.5	0.9125	0.2
$C_{min}(i-j-j)$	1.5	1.1203	0.35
$C_{max}(i-i-j)$	2.0328	3.925	1.4
$C_{max}(j-j-i)$	1.7998	3.3078	1.44
$C_{max}(i-j-i)$	2.4073	3.7191	2.8683
$C_{max}(i-j-j)$	2.3557	1.6912	1.4
$\rho_0(j)/\rho_0(i)$	18.00[a]	1.00	18.00

[a] Reference [38].

by both the models whereas the elastic constants were somewhat underpredicted by the new model in comparison with the Kim model. The exact reproduction of these elastic constants was not the focus of the new model, as there are multiple CuTi phases that grow under the same growth conditions [88,93], and Cu/TiN interfacial properties were given higher weight in the model fitting.

3.2.3. CuN binary systems

The properties of experimentally synthesized Cu_3N ($D0_9$, the structure of anti-ReO_3 (α), space group $Pm3m$) [94] as well as a hypothetical B1-type (NaCl) CuN structure were considered for fitting the CuN model. $\Delta_{mix}H$ and E_S were calculated using DFT. To the best of our knowledge, there are no MEAM models available for CuN. The reproduced properties are compared with the experimental/DFT target values in Table 6.

Table 4
Values of the properties reproduced by the new TiN binary model after fitting, compared with the experimental/DFT results and the values given by the Kim et al. [38] model.

Property	System		Expt/DFT	Kim et al.	This work
Lattice constants (Å)	TiN	a	4.24[a]	4.24	4.24
	Ti_2N	a	4.943[a]	4.785	5.112
		c	3.036[a]	3.047	2.884
$\Delta_{mix}H$ (eV/atom)	TiN		−1.74[b]	−1.74	−1.74
	Ti_2N		−1.38[b]	−1.63	−1.15
Elastic Constants and Moduli (GPa)	TiN	C_{11}	625[c]	659.37	635.40
		C_{12}	165[c]	150.36	151.81
		C_{44}	163[c]	183.39	151.81
		Young's (E)	463*, 469[c, d]	515.21	466.47
		Shear (G)	179[d, e]	209.15	191.48
		Bulk (B)	292[b], 233[d]	320.03	275.78
E_S (J/m^2)	TiN	(001)	1.38[b, f]	1.2717	1.7725
		(110)	2.59–2.86[b, g]	2.4268	2.6170
		(111)	3.32*,3.62[b, f]	3.6362	3.3128
WoA (J/m^2)	Ti/TiN		7.01*	9.9	7.6697
Dimensions of the Interfacial System (Å)	Ti(0001)/ TiN(111)	X‖[$\bar{1}$$\bar{1}$20]	5.9716*	5.9527	5.9303
		Y‖[1100]	5.1591*	5.1598	5.1358

* DFT calculated in the present work.
[a] Reference [77].
[b] Reference [38].
[c] Reference [78].
[d] Reference [49].
[e] Reference [79].
[f] Reference [80].
[g] Reference [81].

3.3. CuTiN ternary model

There are only six ternary interaction parameters for CuTiN, which are given in Table 7. Along with the ternary parameters, the binary CuN and CuTi parameters were all adjusted to reproduce the properties of the CuTiN ternary systems, while maintaining reasonable agreement for CuN and CuTi properties. The final ternary parameters are listed in Table 7.

The main CuTiN target systems have Cu in contact with the TiN interface, which include three different surface combinations that were found to be stable via DFT calculations. The stability of these interfaces was compared by calculating the WoA for both coherent (denoted type-1) and semi-coherent (type-2) interfaces. These include interfaces studied previously: type-1 Cu(001)/TiN(111) and type-2 Cu(111)/TiN(111) [51]. Also, we studied a type-1 Cu(001)/TiN(001) interface with an orientational relation as follows: $X\|[110]_{Cu}\|[110]_{TiN}$; $Y\|\left[1\bar{1}0\right]_{Cu}\|\left[1\bar{1}0\right]_{TiN}$ and $Z \| [001]_{Cu} \| [001]_{TiN}$ [96]. A comparison of the WoA between the MEAM model and DFT for these surfaces is given in Table 8, and generally good agreement is achieved between them.

The WoA calculated with the new MEAM model had good agreement with DFT for type-1 coherent systems, while under-predicting for type-2 semi-coherent system. However, the relative stability of these interfaces in terms of the WoA values were well preserved by the model by reproducing the order correctly, predicting the type-2 system to be the most stable and type-1 Cu(001)/TiN(001) to be the least stable of the three systems.

We considered the two systems with the highest WoA, type-1 Cu(001)/TiN(111) and type-2 Cu(111)/TiN(111), and parameterized the MEAM model to the DFT derived GSFE between their chemical interfaces (P = 0). A comparison of the MEAM and DFT results for the 2D GSFE of the type-1 Cu(001)/TiN(111) interface is given in Fig. 6 (a) and (b). The GSFE was somewhat different than the other systems due to the mismatch between surfaces. The MEAM model reproduced this feature, but some modest differences between the MEAM and DFT results can be observed. The type-2 Cu(111)/TiN(111) interface has been studied experimentally [60–63]. Due to the fact that it is larger and semi-coherent, its GSFE was calculated in one dimension. A comparison between the MEAM model and DFT for the 1D GSFE for type-2 Cu(111)/TiN(111) is given in Fig. 6(c). As can be observed, there were two peaks in the GSFE between each minimum in energy. The MEAM model reproduced one of the peaks fairly well, giving a similar overall energy barrier for the GSFE, but overestimated the smaller peak.

3.4. MDN structure and theoretical shear strength of semi-coherent interfaces

The energetics and the shear response of interfacial systems have been found to have strong links with the location and the structure of misfit dislocation network (MDN) [25,64,65,97]. To this end, we evaluate the MDN structures present at the interfacial regions of Ti/TiN and Cu/TiN systems, and investigate their impact on the shear response of these systems using our new MEAM model. In semi-coherent metal/ceramic interfaces, misfit dislocation networks form due to the lattice mismatch between the metal and the ceramic. To investigate the structure of the MDN and their impact on the energetics, we accommodate the misfit dislocations at successive planes (P) in the metal phase starting from the chemical interface (P = 0 as defined in Fig. 5(d)). For misfit dislocations in P > 0 planes, the atomic layers between the misfit dislocation and the interface are made to be fully coherent with the ceramic. As an example, when misfit dislocations are at the P = 2 plane, the metal atomic layers between that plane and the ceramic [M = 1 and 2 in Fig. 5(d)] are stretched to become coherent with the ceramic. As the misfit dislocations are placed

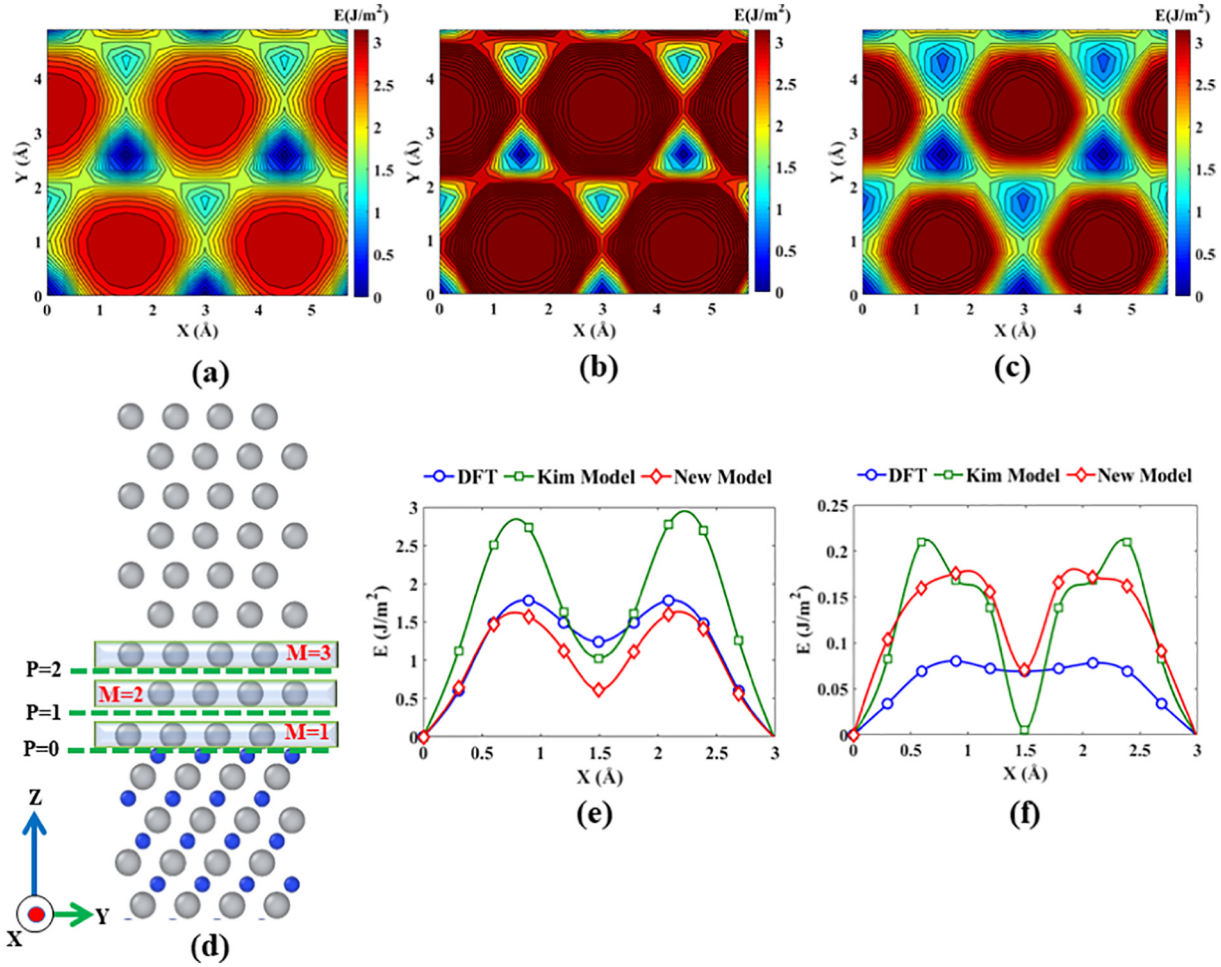

Fig. 5. GSFEs of the chemical interface (P = 0) of Ti/TiN as obtained from (a) DFT, (b) Kim model [38] and (c) our model. (d) Snapshot of Ti/TiN system near with interface with atomic layers and the planes between the layers marked with M and P, respectively. Comparison of the 1-D GSFEs for (e) P = 0 and (f) P = 1 plane of the Ti/TiN interfacial system.

Table 5
Values of the properties reproduced by the new CuTi binary model after fitting, compared with the experimental/DFT results and the values given by the Kim et al. [39] model.

Property	System		Expt/DFT	Kim et al.	This work
Lattice constants (Å)	γ-CuTi	*a*	3.107[a]	3.132	3.126
		c	5.919	6.257	5.975
	$CuTi_2$	*a*	2.943[a]	3.29	2.90
		c	10.784	9.14	11.04
	Cu_3Ti	*a*	5.162[c], 5.45[b]	5.96	5.34
		b	4.347[c], 4.307[b]	4.33	4.34
		c	4.531[c], 4.426[b]	4.47	4.61
	β-Cu_4Ti	*a*	4.522[b]	4.75	4.59
		b	4.344	4.11	4.32
		c	12.897	14.45	13.15
$\Delta_{mix}H$ (eV/atom)	γ-CuTi		−0.115[d]	−0.112	−0.156
			−0.151[*]		
	$CuTi_2$		−0.091[e]	−0.067	−0.147
			−0.143[*]		
Elastic Constants (GPa)	γ-CuTi	C_{11}	176.16[*]	196.46	128.56
		C_{12}	93.64[*]	60.32	77.657
		C_{13}	112.13[*]	101.82	79.37
		C_{33}	175.59[*]	213.30	163.58
		C_{44}	59.73[*]	91.81	39.324
		C_{66}	66.37[*]	115.38	72.82
E_S (J/m²)	γ-CuTi	(001)	2.51[*]	1.81	1.99
		(110)	1.79[*]	1.48	1.53
		(111)	2.05[*]	1.69	1.69

[*] DFT-calculated in the present work.
[a] Reference [83].
[b] Reference [84].
[c] Reference [85].
[d] Reference [86].
[e] Reference [87].

further away from the interface, more and more layers are made coherent with the ceramic.

3.4.1. Ti/TiN interfaces

In Fig. 7(a), the interfacial energy of Ti/TiN is plotted as a function of the MDN location. The plot is normalized to the interfacial energy of a completely coherent Ti/TiN structure. Interfacial energy is the highest when a misfit dislocation is present at the interface, and lowest when it is present one Ti layer away from the interface because of the low stacking fault energy at that layer. This can be observed in DFT calculations of Ti/TiN interfaces [51,52]. As the MDN is moved away from the interface, the elastic energy of the MDN decreases with its diminishing stress field. In addition, the elastic energy of the coherent layers sandwiched between the MDN and the chemical interface increases, as more layers are strained to achieve coherency [25]. This results in a

Table 6
Comparison between the properties reproduced by the new model in this work and the experimental/DFT target values.

Property	System		Expt/DFT	This work
Lattice constants (Å)	Cu_3N	*a*	3.819[a]	3.94
	CuN	*a*	4.1479[*]	3.98
$\Delta_{mix}H$ (eV/atom)	Cu_3N		−3.646[*]	−3.652
	CuN		−4.529[*]	−4.428
E_S (J/m²)	Cu_3N	(001)	1.13[*]	0.46
		(111)	1.21[*]	0.75

[*] DFT-calculated in the present work.
[a] Reference [95].

Table 7
Ternary parameters for CuTiN after fitting.

Parameters	Value
$C_{min}(Cu-N-Ti)$	0.4617
$C_{min}(Cu-Ti-N)$	1.3982
$C_{min}(Ti-N-Cu)$	0.6637
$C_{max}(Cu-N-Ti)$	2.4612
$C_{max}(Cu-Ti-N)$	2.2499
$C_{max}(Ti-N-Cu)$	1.6901

Table 8
Comparison of WoA calculated with DFT and our MEAM model for Cu/TiN interfacial systems.

System	DFT	MEAM
Type-1 Cu(001)/TiN(111)	1.90	1.74
Type-1 Cu(001)/TiN(001)	0.62	0.65
Type-2 Cu(111)/TiN(111)	3.17	2.41

steady but small (around 0.15 J/m^2) increase in the interfacial energy as the MDN is moved away from P = 1.

Interfacial strength calculated from our new model and the Lee model is illustrated in Fig. 7(b) as a function of MDN location. Both MEAM models predict low shear strength when MDN is one or two layers away from the interface agreeing with Zhang et al. [25]. When the MDN is in the first few layers, our model estimated lower shear strength than the Lee model for both OR structures. At P = 0, the GSFE barriers were much higher for the Lee model compared to both DFT and our model [see Fig. 5(e)], which may have caused a larger estimation of the shear strength. MDN structures at P = 1 obtained from the Lee model and our model are shown in Fig. 7(c-d). Due to the lower GSFE barriers with our model, which were fit to DFT [see Fig. 5(e)], the nodes are larger than with the Lee model. These larger nodes offer little to no pinning to the dislocation glide for P = 1 and P = 2, resulting in relatively unimpeded translation of MDN with shear loading. The effect of this is manifested in the lower shear strength with our model.

From the bulk density of Ti, the number of Ti atoms in two atomic layers can be estimated to be 2.66×10^{19} m^{-2} (See Sec. S1. in the supplementary information). The difference in energy between the system with MDN at P = 1 and the system with MDN several layers away is approximately 0.15 J/m^2, which amounts to 35 meV per Ti atom. This is close to the thermal energy at room temperature (26 meV, assuming T = 300 K). Hence, small change in growth temperature may move the location of the MDN further away from P = 1 causing the first few interfacial layers to be coherent. If this is the case, the theoretical shear strengths obtained from our model for MDN a few layers away from the chemical interface would agree with the experimental shear strength ranging between 1200 and 1800 MPa, measured with metal/ceramic interfaces of a similar interfacial system, Ti/CrN [25].

3.4.2. Cu/TiN semi-coherent interfaces

Misfits accommodated at the chemical interface (P = 0) of Cu(111)/TiN(111) results in small regions of coherency after relaxation. An analysis of the first Cu layer (M = 1) illustrated in Fig. 8(a), reveals large core-widths of the dislocations (green regions) between small coherent regions (blue regions). This is consistent with the small GSFE barrier at the Cu/TiN interface. The atomic arrangement of the blue coherent region in Fig. 8(a) are shown in Fig. 8(b). The MDN structure in the P = 1 layer exhibits zigzag dislocation lines [see Fig. 8(c)] which may correspond to the competition between the coherency stress and the large elastic energy of the MDN (due to larger GSFE barrier in this layer [51]) accommodated at the same single atomic layer M = 1. For misfits placed further away from the interface in the Cu bulk, the spiral pattern in its MDN structure becomes more prominent [see Fig. 8(d)]. Such spiral patterns for metal/metal semi-coherent (111) surfaces have been reported in previous work [64,98,99]. Shown in Fig. 8(e),

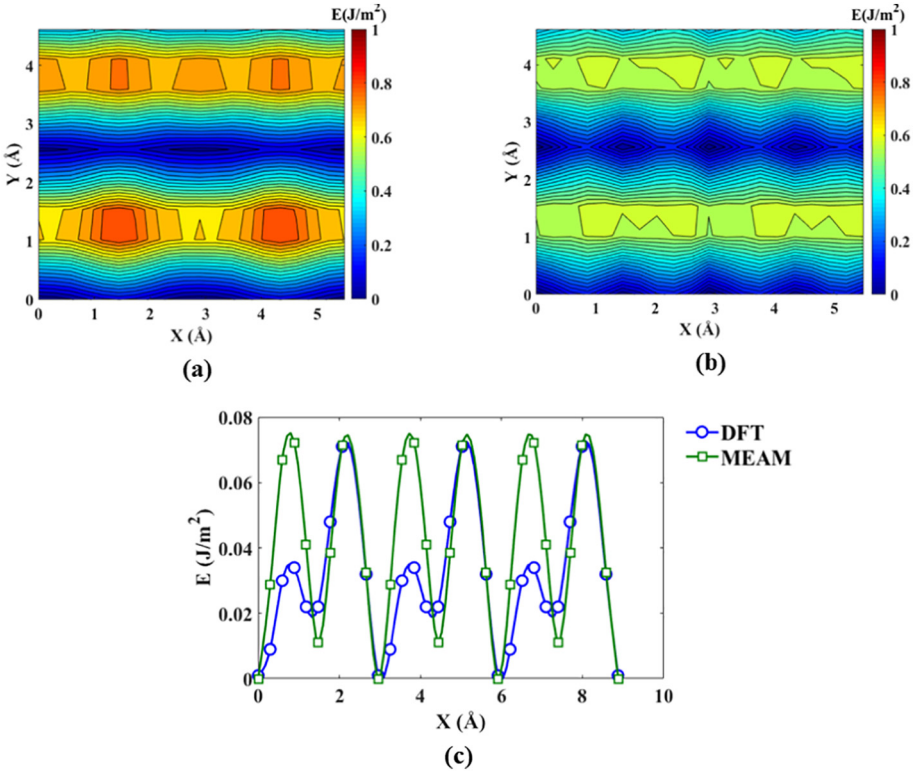

Fig. 6. *P* = 0 GSFE surfaces for type-1 Cu/TiN interfaces calculated with (a) DFT and (b) our MEAM model. (c) Comparison between the P = 0 1-D GSFE's of type-2 Cu/TiN.

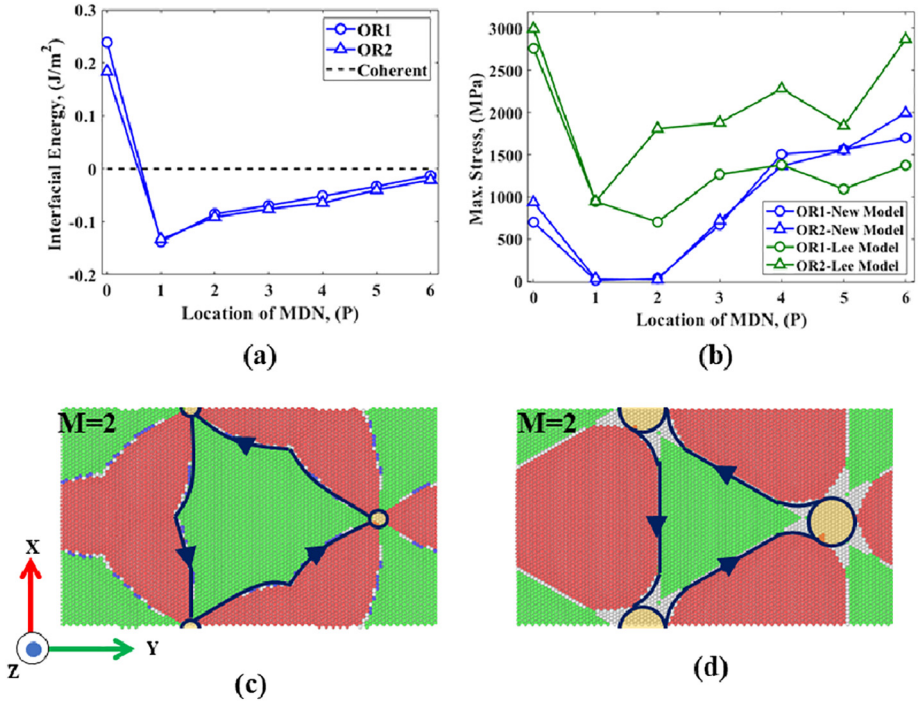

Fig. 7. Plots of (a) interfacial energy normalized to the energy of the coherent structure and (b) theoretical shear strength; both as a function of MDN location. MDN structure when the misfit is at P = 1 (between M = 1 and 2) for OR1 with (c) Lee model and (d) our model. Green, red and white atoms are in local FCC, HCP and overlap environment, respectively. The dislocation line senses are drawn in deep blue colour with the circles identifying the nodes. (For interpretation of the references to colour in this figure legend, the reader is referred to the web version of this article.)

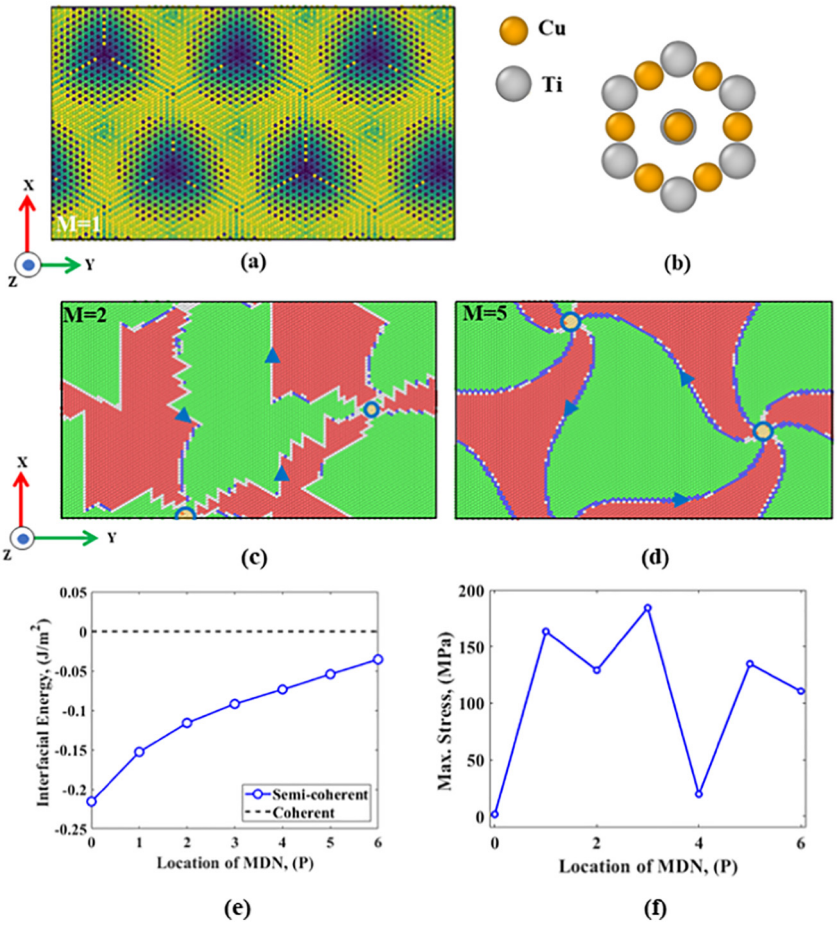

Fig. 8. (a) Snapshot of the first Cu layer when the misfit is deposited at the chemical interface $P = 0$. The colors from blue to green indicate the coherency of the atom with blue being the most coherent. (b) Atomic arrangement of the coherent region. MDN structures when the misfit is at the (c) P = 1 and (d) $P = 4$ planes. Green and red atoms are in local FCC and HCP environments, respectively. Plots of (e) interfacial energy normalized to the coherent interfacial energy and (f) theoretical shear strength, both as a function of MDN location at the Cu/TiN interface. (For interpretation of the references to colour in this figure legend, the reader is referred to the web version of this article.)

the interfacial energy steadily rises as the MDNs are located further away from the interface since more layers undergo strain to achieve coherency, approaching the energy of a fully coherent Cu phase (dashed line). The MDN structures of other layers are shown in Fig. S2 in the supplementary materials.

As discussed earlier, the low GSFE barriers at the interface lead to larger core-width of the dislocations at M = 1. Such MDN structures result in a very small shear strength of around 1.65 MPa, showing reasonable agreement with the experimental peeling strength of thin PVD-Cu (111) films from TiN/Polyimide (2.2 ± 0.3 MPa) [100]. The experimental 'peeling' suggested in Reference [100] is somewhat analogous to our simulations since the Cu film breaks off TiN with a loading parallel to the interface. The shear strength calculated with the new model rapidly increases as the MDN is moved to the next layer, likely due to the much higher GSFE barrier height there [51]. As the MDN moves farther away from the interface, the shear strength oscillates up and down. In particular, the MDN at P = 4 causes a near perfect spiral pattern that may have caused the shear strength to be the lowest among the systems that have misfits away from the interface.

4. Conclusion

A second nearest neighbor modified embedded atom method interatomic potential was developed to study Ti/TiN and Cu/TiN interfaces. A genetic algorithm scheme in combination with a minimization procedure was utilized to fit MEAM potential parameters to an array of physical properties. First, pure Ti and Cu models were developed and after satisfactory reproduction of their properties, several phases of CuTi, TiN and CuN binary systems were parameterized. Finally, ternary parameters for CuTiN were optimized for several Cu/TiN systems with different interfacial orientation relations. To the best of our knowledge, there are no previously developed MEAM potentials available for CuTiN ternary systems.

The newly developed model was used to perform MD simulations aimed at understanding the MDN structure and their effect on the mechanical response of Ti(0001)/TiN(111) and Cu(111)/TiN(111) interfacial systems. Stable Ti/TiN systems were achieved when the MDN was away from the interface. Very small fluctuations in energy, comparable to the thermal energy of atoms at room temperature, were observed as the MDN was stationed further away into the Ti bulk. Theoretical shear strength calculated with our model qualitatively agrees with the experimental measurements on systems of similar configuration [25], when the MDN are a few layers away from the interface. For Cu/TiN, most stable system consisted of MDN at the interface. Near the interface, the MDN structures were more jagged whereas away from the interface, a spiral pattern, previously observed in metal/metal (111) semi-coherent systems, was more dominant. Upon shear loading, the strength of the most stable system had reasonable agreement with experiment.

Declaration of Competing Interest

None.

Acknowledgements

The current work is funded by the United States National Science Foundation under cooperative agreement #OIA-1541079. The high performance computing resources provided by the Louisiana Optical Network Infrastructure (https://loni.org) were used for this work.

Appendix A. Supplementary data

Supplementary data to this article can be found online at https://doi.org/10.1016/j.matdes.2020.109123.

References

[1] J.S. Moya, S. Lopez-Esteban, C. Pecharromán, The challenge of ceramic/metal microcomposites and nanocomposites, Prog. Mater. Sci. 52 (2007) 1017–1090, https://doi.org/10.1016/j.pmatsci.2006.09.003.
[2] J. Carmai, F. Dunne, Chapter 11 Manufacture of ceramic fibre metal matrix composites, Met. Ceram. Matrix Compos, 2004.
[3] M. Halbig, M. Jaskowiak, J. Kiser, D. Zhu, Evaluation of ceramic matrix composite technology for aircraft turbine engine applications, 51st AIAA Aerosp. Sci. Meet. Incl. New Horizons Forum Aerosp. Expo, American Institute of Aeronautics and Astronautics, Reston, Virigina, 2013. https://doi.org/10.2514/6.2013-539.
[4] F. Dunne, B. Cantor, I. Stone, Metal and Ceramic Matrix Composites, Taylor & Francis, 2003. https://doi.org/10.1201/9781420033977.
[5] K.U. Kainer (Ed.), Metal Matrix Composites, Wiley-VCH Verlag GmbH & Co. KGaA, Weinheim, FRG, 2006. https://doi.org/10.1002/3527608117.
[6] J. Horník, S. Krum, D. Tondl, M. Puchnin, P. Sachr, L. Cvrček, Multilayer coatings Ti/TiN, Cr/CrN AND W/WN deposited by magnetron sputtering for improvement of adhesion to base materials, Acta Polytech. 55 (2015) 388–392, https://doi.org/10.14311/AP.2015.55.0388.
[7] F.-Y. Lin, A. Chernatynskiy, J.C. Nino, J.L. Jones, R. Hennig, S.B. Sinnott, Role of composition and structure on the properties of metal/multifunctional ceramic interfaces, J. Appl. Phys. 120 (2016), 045310, https://doi.org/10.1063/1.4959074.
[8] V. Bonu, M. Jeevitha, V. Praveen Kumar, H.C. Barshilia, Nanolayered multilayer Ti/TiN coatings: role of bi-layer thickness and annealing on solid particle erosion behaviour at elevated temperature, Surf. Coat. Technol. 357 (2019) 204–211, https://doi.org/10.1016/j.surfcoat.2018.10.007.
[9] W. Yang, G. Ayoub, I. Salehinia, B. Mansoor, H. Zbib, The effect of layer thickness ratio on the plastic deformation mechanisms of nanoindented Ti/TiN nanolayered composite, Comput. Mater. Sci. 154 (2018) 488–498, https://doi.org/10.1016/j.commatsci.2018.08.021.
[10] T. Sun, X. Wu, R. Wang, W. Li, Q. Liu, First-principles study on the adhesive properties of Al/TiC interfaces: revisited, Comput. Mater. Sci. 126 (2017) 108–120, https://doi.org/10.1016/j.commatsci.2016.09.024.
[11] G. Pilania, B.J. Thijsse, R.G. Hoagland, I. LaziÃ, S.M. Valone, X.Y. Liu, Revisiting the Al/Al 2 O 3 interface: coherent interfaces and misfit accommodation, Sci. Rep. 4 (2014) 1–9, https://doi.org/10.1038/srep04485.
[12] S.K. Yadav, R. Ramprasad, J. Wang, A. Misra, X.Y. Liu, First-principles study of Cu/TiN and Al/TiN interfaces: weak versus strong interfaces, Model. Simul. Mater. Sci. Eng. 22 (2014). https://doi.org/10.1088/0965-0393/22/3/035020.
[13] D.H.R. Fors, G. Wahnström, Theoretical study of interface structure and energetics in semicoherent Fe(001)/MX(001) systems (M=Sc, Ti, V, Cr, Zr, Nb, Hf, Ta; X=C or N), Phys. Rev. B - Condens. Matter Mater. Phys. 82 (2010) 1–13, https://doi.org/10.1103/PhysRevB.82.195410.
[14] M. Damadam, S. Shao, G. Ayoub, H.M. Zbib, Recent advances in modeling of interfaces and mechanical behavior of multilayer metallic/ceramic composites, J. Mater. Sci. 53 (2018) 5604–5617, https://doi.org/10.1007/s10853-017-1704-3.
[15] I. Salehinia, S. Shao, J. Wang, H.M. Zbib, Interface structure and the inception of plasticity in Nb/NbC nanolayered composites, Acta Mater. 86 (2015) 331–340, https://doi.org/10.1016/j.actamat.2014.12.026.
[16] X. Guo, Y. Zhang, Y.-G. Jung, L. Li, J. Knapp, J. Zhang, Ideal tensile strength and shear strength of ZrO2(111)/Ni(111) ceramic-metal interface: a first principle study, Mater. Des. 112 (2016) 254–262, https://doi.org/10.1016/j.matdes.2016.09.073.
[17] A. Sazgar, M.R. Movahhedy, M. Mahnama, S. Sohrabpour, A molecular dynamics study of bond strength and interface conditions in the Al/Al2O3 metal-ceramic composites, Comput. Mater. Sci. 109 (2015) 200–208, https://doi.org/10.1016/j.commatsci.2015.07.024.
[18] L. Chen, J. Paulitsch, Y. Du, P.H. Mayrhofer, Thermal stability and oxidation resistance of Ti-Al-N coatings, Surf. Coat. Technol. 206 (2012) 2954–2960, https://doi.org/10.1016/j.surfcoat.2011.12.028.
[19] P. S., D. S.C, Single layer and multilayer wear resistant coatings of (Ti,Al)N: a review, Mater. Sci. Eng. A 342 (2003) 58–79, https://doi.org/10.1016/S0921-5093(02)00259-9.
[20] A.R. Shugurov, M.S. Kazachenok, Mechanical properties and tribological behavior of magnetron sputtered TiAlN/TiAl multilayer coatings, Surf. Coat. Technol. 353 (2018) 254–262, https://doi.org/10.1016/j.surfcoat.2018.09.001.
[21] M.T. Vieira, A.S. Ramos, Influence of ductile interlayers on the mechanical performance of tungsten nitride coatings, J. Mater. Process. Technol. 92–93 (1999) 156–161, https://doi.org/10.1016/S0924-0136(99)00235-6.
[22] J.M. Lackner, L. Major, M. Kot, Microscale interpretation of tribological phenomena in Ti/TiN soft-hard multilayer coatings on soft austenite steel substrates, Bull. Polish Acad. Sci. Tech. Sci. 59 (2011) 343–356, https://doi.org/10.2478/v10175-011-0042-x.
[23] W. Tillmann, E. Vogli, S. Momeni, Mechanical and tribological properties of Ti/TiAlN duplex coatings on high and low alloy tool steels, Vacuum 84 (2009) 387–392, https://doi.org/10.1016/j.vacuum.2009.08.001.
[24] E. Vogli, W. Tillmann, U. Selvadurai-Lassl, G. Fischer, J. Herper, Influence of Ti/TiAlN-multilayer designs on their residual stresses and mechanical properties, Appl. Surf. Sci. 257 (2011) 8550–8557, https://doi.org/10.1016/j.apsusc.2011.05.013.
[25] X. Zhang, B. Zhang, Y. Mu, S. Shao, C.D. Wick, B.R. Ramachandran, W.J. Meng, Mechanical failure of metal/ceramic interfacial regions under shear loading, Acta Mater. 138 (2017) 224–236, https://doi.org/10.1016/j.actamat.2017.07.053.
[26] W.J. Lee, Y.S. Lee, S.K. Rha, Y.J. Lee, K.Y. Lim, Y.D. Chung, C.N. Whang, Adhesion and interface chemical reactions of Cu/polyimide and Cu/TiN by XPS, Appl. Surf. Sci. 205 (2002) 128–136, https://doi.org/10.1016/S0169-4332(02)01016-4.

[27] M.Y. Kwak, D.H. Shin, T.W. Kang, K.N. Kim, Characteristics of TiN barrier layer against Cu diffusion, Thin Solid Films 339 (1999) 290–293, https://doi.org/10.1016/S0040-6090(98)01074-8.

[28] T.Z. Kattamis, On the evaluation of adhesion of coatings by automatic scratch testing, J. Adhes. Sci. Technol. 7 (1993) 783–799, https://doi.org/10.1163/156856193x00439.

[29] M.D. Drory, J.W. Hutchinson, Measurement of the adhesion of a brittle film on a ductile substrate by indentation, Proc. R. Soc. A Math. Phys. Eng. Sci. 452 (1996) 2319–2341, https://doi.org/10.1098/rspa.1996.0124.

[30] K. Matouš, M.G.D. Geers, V.G. Kouznetsova, A. Gillman, A review of predictive nonlinear theories for multiscale modeling of heterogeneous materials, J. Comput. Phys. 330 (2017) 192–220, https://doi.org/10.1016/j.jcp.2016.10.070.

[31] M. Damadam, S. Shao, I. Salehinia, G. Ayoub, H.M. Zbib, Molecular dynamics simulations of mechanical behavior in nanoscale ceramic–metallic multilayer composites, Mater. Res. Lett. 5 (2017) 306–313, https://doi.org/10.1080/21663831.2016.1275864.

[32] W. Yang, G. Ayoub, I. Salehinia, B. Mansoor, H. Zbib, Multiaxial tension/compression asymmetry of Ti/TiN nano laminates: MD investigation, Acta Mater. 135 (2017) 348–360, https://doi.org/10.1016/j.actamat.2017.06.034.

[33] H. Yang, L. Zhu, R. Zhang, J. Zhou, Z. Sun, Shearing dominated by the coupling of the interfacial misfit and atomic bonding at the FCC (111) semi-coherent interfaces, Mater. Des. 186 (2020) 108294, https://doi.org/10.1016/j.matdes.2019.108294.

[34] X. Zhou, W. Bu, S. Song, F. Sansoz, X. Huang, Multiscale modeling of interfacial mechanical behaviours of SiC/Mg nanocomposites, Mater. Des. 182 (2019) 108093, https://doi.org/10.1016/j.matdes.2019.108093.

[35] B.-J. Lee, T.-H. Lee, S.-J. Kim, A modified embedded-atom method interatomic potential for the Fe–N system: a comparative study with the Fe–C system, Acta Mater. 54 (2006) 4597–4607, https://doi.org/10.1016/j.actamat.2006.06.003.

[36] Y.-M. Kim, B.-J. Lee, M.I. Baskes, Modified embedded-atom method interatomic potentials for Ti and Zr, Phys. Rev. B 74 (2006), 014101, https://doi.org/10.1103/PhysRevB.74.014101.

[37] B. Jelinek, S. Groh, M.F. Horstemeyer, J. Houze, S.G. Kim, G.J. Wagner, A. Moitra, M.I. Baskes, Modified embedded atom method potential for Al, Si, Mg, Cu, and Fe alloys, Phys. Rev. B 85 (2012) 245102, https://doi.org/10.1103/PhysRevB.85.245102.

[38] Y. Kim, B. Lee, Modified embedded-atom method interatomic potentials for the Ti–C and Ti–N binary systems, Acta Mater. 56 (2008) 3481–3489, https://doi.org/10.1016/j.actamat.2008.03.027.

[39] Y.-M. Kim, B.-J. Lee, A semi-empirical interatomic potential for the Cu–Ti binary system, Mater. Sci. Eng. A 449–451 (2007) 733–736, https://doi.org/10.1016/j.msea.2006.02.345.

[40] M.I. Baskes, R.A. Johnson, Modified embedded atom potentials for HCP metals, Model. Simul. Mater. Sci. Eng. 2 (1994) 147–163, https://doi.org/10.1088/0965-0393/2/1/011.

[41] M.I. Baskes, J.S. Nelson, A.F. Wright, Semiempirical modified embedded-atom potentials for silicon and germanium, Phys. Rev. B 40 (1989) 6085–6100, https://doi.org/10.1103/PhysRevB.40.6085.

[42] M.I. Baskes, Modified embedded-atom potentials for cubic materials and impurities, Phys. Rev. B 46 (1992) 2727–2742, https://doi.org/10.1103/PhysRevB.46.2727.

[43] M.I. Baskes, Application of the embedded-atom method to covalent materials: a Semiempirical potential for silicon, Phys. Rev. Lett. 59 (1987) 2666–2669, https://doi.org/10.1103/PhysRevLett.59.2666.

[44] B.-J. Lee, J.-H. Shim, M.I. Baskes, Semiempirical atomic potentials for the fcc metals cu, Ag, Au, Ni, Pd, Pt, Al, and Pb based on first and second nearest-neighbor modified embedded atom method, Phys. Rev. B 68 (2003) 144112, https://doi.org/10.1103/PhysRevB.68.144112.

[45] B.-J. Lee, M.I. Baskes, H. Kim, Y. Koo Cho, Second nearest-neighbor modified embedded atom method potentials for bcc transition metals, Phys. Rev. B 64 (2001) 184102, https://doi.org/10.1103/PhysRevB.64.184102.

[46] B.-J. Lee, M.I. Baskes, Second nearest-neighbor modified embedded-atom-method potential, Phys. Rev. B 62 (2000) 8564–8567, https://doi.org/10.1103/PhysRevB.62.8564.

[47] P. Liu, X. Han, D. Sun, Q. Wang, Development and application of a ternary Ti-Al-N interatomic potential for Ti2AlN/TiAl composite, J. Alloys Compd. 745 (2018) 63–74, https://doi.org/10.1016/j.jallcom.2018.02.168.

[48] J.H. Rose, J.R. Smith, F. Guinea, J. Ferrante, Universal features of the equation of state of metals, Phys. Rev. B 29 (1984) 2963–2969, https://doi.org/10.1103/PhysRevB.29.2963.

[49] Y. Yang, H. Lu, C. Yu, J.M. Chen, First-principles calculations of mechanical properties of TiC and TiN, J. Alloys Compd. 485 (2009) 542–547, https://doi.org/10.1016/j.jallcom.2009.06.023.

[50] C. Wu, B.-J. Lee, X. Su, Modified embedded-atom interatomic potential for Fe-Ni, Cr-Ni and Fe-Cr-Ni systems, Calphad 57 (2017) 98–106, https://doi.org/10.1016/j.calphad.2017.03.007.

[51] A.S. Mohammad Miraz, S. Sun, S. Shao, W.J. Meng, B.R. Ramachandran, C.D. Wick, Computational study of metal/ceramic interfacial adhesion and barriers to shear displacement, Comput. Mater. Sci. 168 (2019) 104–115, https://doi.org/10.1016/j.commatsci.2019.06.006.

[52] A.S.M. Miraz, E. Williams, W.J. Meng, B.R. Ramachandran, C.D. Wick, Improvement of Ti/TiN interfacial shear strength by doping – a first principles density functional theory study, Appl. Surf. Sci. 517 (2020) 146185, https://doi.org/10.1016/j.apsusc.2020.146185.

[53] J.P. Perdew, K. Burke, M. Ernzerhof, Generalized gradient approximation made simple, Phys. Rev. Lett. 77 (1996) 3865–3868, https://doi.org/10.1103/PhysRevLett.77.3865.

[54] G. Kresse, J. Furthmüller, Efficient iterative schemes for ab initio total-energy calculations using a plane-wave basis set, Phys. Rev. B 54 (1996) 11169–11186, https://doi.org/10.1103/PhysRevB.54.11169.

[55] J. Hafner, Ab-initio simulations of materials using VASP: density-functional theory and beyond, J. Comput. Chem. 29 (2008) 2044–2078, https://doi.org/10.1002/jcc.21057.

[56] H.J. Monkhorst, J.D. Pack, Special points for Brillouin-zone integrations, Phys. Rev. B 13 (1976) 5188–5192, https://doi.org/10.1103/PhysRevB.13.5188.

[57] S. Plimpton, Fast parallel algorithms for short-range molecular dynamics, J. Comput. Phys. 117 (1995) 1–19, https://doi.org/10.1006/jcph.1995.1039.

[58] W.G. Hoover, Canonical dynamics: equilibrium phase-space distributions, Phys. Rev. A 31 (1985) 1695–1697, https://doi.org/10.1103/PhysRevA.31.1695.

[59] S. Nosé, A unified formulation of the constant temperature molecular dynamics methods, J. Chem. Phys. 81 (1984) 511–519, https://doi.org/10.1063/1.447334.

[60] K. Abe, Y. Harada, H. Onoda, Study of crystal orientation in Cu film on TiN layered structures, J. Vac. Sci. Technol. B Microelectron. Nanom. Struct. 17 (1999) 1464, https://doi.org/10.1116/1.590775.

[61] K. Abe, Y. Harada, M. Yoshimaru, H. Onoda, Texture and electromigration performance in damascene interconnects formed by reflow sputtered Cu film, J. Vac. Sci. Technol. B Microelectron. Nanom. Struct. 22 (2004) 721, https://doi.org/10.1116/1.1676618.

[62] M. Sekiguchi, H. Sato, T. Harada, R. Etoh, Highly ⟨111⟩ textured Cu film formation on CVD-TiN film by Ti underlayer and Ar sputter etch for damascene interconnection, Proc. IEEE 1999 Int. Interconnect Technol. Conf. (Cat. No.99EX247), IEEE 2020, pp. 116–118, https://doi.org/10.1109/IITC.1999.787095.

[63] K. Abe, Y. Harada, H. Onoda, Cu crystallographic texture control in Cu/refractory-metal layered structure as interconnects, Appl. Phys. Lett. 71 (1997) 2782–2784, https://doi.org/10.1063/1.120132.

[64] S. Shao, J. Wang, I.J. Beyerlein, A. Misra, Glide dislocation nucleation from dislocation nodes at semi-coherent {111} Cu–Ni interfaces, Acta Mater. 98 (2015) 206–220, https://doi.org/10.1016/j.actamat.2015.07.044.

[65] J. Wang, R.G. Hoagland, J.P. Hirth, A. Misra, Atomistic simulations of the shear strength and sliding mechanisms of copper–niobium interfaces, Acta Mater. 56 (2008) 3109–3119, https://doi.org/10.1016/j.actamat.2008.03.003.

[66] A. Tunde Raji, S. Scandolo, R. Mazzarello, S. Nsengiyumva, M. Härting, D. Thomas Britton, Ab initio pseudopotential study of vacancies and self-interstitials in hcp titanium, Philos. Mag. 89 (2009) 1629–1645, https://doi.org/10.1080/14786430903019032.

[67] W. Schüle, Properties of vacancies in copper determined by electrical resistivity techniques, Zeitschrift Für Met. 89 (1998) 672–677.

[68] T. Hehenkamp, W. Berger, J.-E. Kluin, C. Lüdecke, J. Wolff, Equilibrium vacancy concentrations in copper investigated with the absolute technique, Phys. Rev. B 45 (1992) 1998.

[69] F.R. de Boer, R. Boom, W.C.M. Mattens, A.R. Miedema, A.K. Niessen, Cohesion in Metals - Transition Metal Alloys, North-Holland Physics Publishing, Amsterdam, 1988.

[70] W.R. Tyson, W.A. Miller, Surface free energies of solid metals: estimation from liquid surface tension measurements, Surf. Sci. 62 (1977) 267–276, https://doi.org/10.1016/0039-6028(77)90442-3.

[71] M.P.J. Punkkinen, Q.-M. Hu, S.K. Kwon, B. Johansson, J. Kollár, L. Vitos, Surface properties of 3 d transition metals, Philos. Mag. 91 (2011) 3627–3640, https://doi.org/10.1080/14786435.2011.586953.

[72] W.M. Haynes, CRC Handbook of Chemistry and Physics, CRC press, 2014.

[73] R.B. Ross, Metallic Materials Specification Handbook, Springer US, Boston, MA, 1992https://doi.org/10.1007/978-1-4615-3482-2.

[74] E.S. Fisher, C.J. Renken, Single-crystal elastic moduli and the hcp→ bcc transformation in Ti, Zr, and Hf, Phys. Rev. 135 (1964) A482.

[75] G. Simmons, Single Crystal Elastic Constants and Calculated Aggregate Properties, Southern Methodist Univ Dallas Tex, 1965.

[76] S. Epstein, O. Carlson, The elastic constants of nickel-copper alloy single crystals, Acta Metall. 13 (1965) 487–491, https://doi.org/10.1016/0001-6160(65)90098-2.

[77] J.L. Murray, H.A. Wriedt, in: J.L. Murray (Ed.), Phase Diagrams of Binary Titanium Alloys, 319, ASM Int. Met., Park. OH, USA 1987, p. 327.

[78] J.O. Kim, J.D. Achenbach, P.B. Mirkarimi, M. Shinn, S.A. Barnett, Elastic constants of single-crystal transition-metal nitride films measured by line-focus acoustic microscopy, J. Appl. Phys. 72 (1992) 1805–1811, https://doi.org/10.1063/1.351651.

[79] W.J. Meng, G.L. Eesley, Growth and mechanical anisotropy of TiN thin films, Thin Solid Films 271 (1995) 108–116.

[80] S.V. Dudiy, B.I. Lundqvist, Wetting of TiC and TiN by metals, Phys. Rev. B 69 (2004) 125421, https://doi.org/10.1103/PhysRevB.69.125421.

[81] M. Marlo, V. Milman, Density-functional study of bulk and surface properties of titanium nitride using different exchange-correlation functionals, Phys. Rev. B 62 (2000) 2899–2907, https://doi.org/10.1103/PhysRevB.62.2899.

[82] C. Wu, J. Li, Phase structure of the Ti1Cu1− x Fe x system, Metall. Trans. A. 20 (1989) 981–985, https://doi.org/10.1007/BF02650135.

[83] V.N. Eremenko, Y.I. Buyanov, S.B. Prima, Phase diagram of the system titanium-copper, Sov. Powder Metall. Met. Ceram. 5 (1966) 494–502, https://doi.org/10.1007/BF00775543.

[84] J.L. Murray, The Cu—Ti (copper-titanium) system, Bull. Alloy Phase Diagr. 4 (1983) 81–95, https://doi.org/10.1007/BF02880329.

[85] K.H.J. Buschow, Thermal stability of amorphous Ti-Cu alloys, Acta Metall. 31 (1983) 155–160, https://doi.org/10.1016/0001-6160(83)90075-5.

[86] C. Colinet, A. Pasturel, K.H.J. Buschow, Enthalpies of formation of Ti Cu intermetallic and amorphous phases, J. Alloys Compd. 247 (1997) 15–19, https://doi.org/10.1016/S0925-8388(96)02590-X.

[87] M. Arita, R. Kinaka, M. Someno, Application of the metalhydrogen equilibration for determining thermodynamic properties in the ti-cu system, Metall. Trans. A. 10 (1979) 529–534, https://doi.org/10.1007/BF02658315.
[88] M.R. Akbarpour, F.A. Hesari, Characterization and hardness of TiCu–Ti 2 Cu 3 intermetallic material fabricated by mechanical alloying and subsequent annealing, Mater. Res. Express. 3 (2016), 045004, https://doi.org/10.1088/2053-1591/3/4/045004.
[89] V.N. Eremenko, Y.I. Buyanov, N.M. Panchenko, Polythermal and isothermal sections of the system titanium-copper-silver. Part II, Sov. Powder Metall. Met. Ceram. 9 (1970) 410–414, https://doi.org/10.1007/BF00796511.
[90] S. Chen, Y.-H. Duan, B. Huang, W.-C. Hu, Structural properties, phase stability, elastic properties and electronic structures of Cu–Ti intermetallics, Philos. Mag. 95 (2015) 3535–3553, https://doi.org/10.1080/14786435.2015.1091110.
[91] T. Uzunov, S. Lambov, S. Stojanov, Kinetics of solid-phase interactions in thin-film system with an excess of Cu, Vacuum 47 (1996) 61–65, https://doi.org/10.1016/0042-207X(95)00028-3.
[92] A. Andresen, A. Maeland, Hydrogen absorption in some compounds of MoSi2-type structure, J. Less Common Met. 129 (1987) 115–121, https://doi.org/10.1016/0022-5088(87)90038-5.
[93] T. Uzunov, S. Lambov, S. Stojanov, Kinetics of solid-phase interactions in thin-film system with an excess of Cu, Vacuum 47 (1996) 61–65, https://doi.org/10.1016/0042-207X(95)00028-3.
[94] M.S.H. Suleiman, M.P. Molepo, D.P. Joubert, A theoretical investigation of structural, electronic and optical properties of bulk copper nitrides, J. Alloys Compd. 753 (2018) 576–585, https://doi.org/10.1016/j.jallcom.2018.04.036.
[95] U. Zachwieja, H. Jacobs, Ammonothermalsynthese von kupfernitrid, Cu3N, J. Less Common Met. 161 (1990) 175–184, https://doi.org/10.1016/0022-5088(90)90327-G.
[96] X. Zhang, S. Shao, A.S.M. Miraz, C.D. Wick, B.R. Ramachandran, W.J. Meng, Low temperature growth of Cu thin films on TiN(001) templates: structure and energetics, Materialia. 12 (2020) 100748, https://doi.org/10.1016/j.mtla.2020.100748.
[97] Y. Chen, S. Shao, X.-Y. Liu, S.K. Yadav, N. Li, N. Mara, J. Wang, Misfit dislocation patterns of Mg-Nb interfaces, Acta Mater. 126 (2017) 552–563, https://doi.org/10.1016/j.actamat.2016.12.041.
[98] S. Shao, J. Wang, A. Misra, R.G. Hoagland, Spiral patterns of dislocations at nodes in (111) semi-coherent FCC interfaces, Sci. Rep. 3 (2013) 1–7, https://doi.org/10.1038/srep02448.
[99] S. Shao, J. Wang, A. Misra, Energy minimization mechanisms of semi-coherent interfaces, J. Appl. Phys. 116 (2014). https://doi.org/10.1063/1.4889927.
[100] T.X. Liang, Y.Q. Liu, Z.Q. Fu, T.Y. Luo, K.Y. Zhang, Diffusion and adhesion properties of Cu films on polyimide substrates, Thin Solid Films 473 (2005) 247–251, https://doi.org/10.1016/j.tsf.2004.07.073.